


Article

In Situ Infrared Spectra for Hydrous Forsterite up to 1243 K: Hydration Effect on Thermodynamic Properties

Dan Liu ¹, Sha Wang ¹, Joseph R. Smyth ², Junfeng Zhang ^{1,3}, Xiang Wang ¹, Xi Zhu ¹ and Yu Ye ^{1,*} 

¹ State Key Laboratory of Geological Processes and Mineral Resources, China University of Geosciences, Wuhan 430074, China

² Department of Geological Sciences, University of Colorado, Boulder, CO 80309, USA

³ School of Earth Sciences, China University of Geosciences, Wuhan 430074, China

* Correspondence: yeyu@cug.edu.cn

Received: 26 July 2019; Accepted: 21 August 2019; Published: 25 August 2019



Abstract: Hydrogen substitution has significant effect on the physical properties of olivine, the most abundant mineral in the upper mantle. We collected high-temperature polarized Fourier Transform infrared (FTIR) spectra on hydrous forsterite (Mg-pure olivine) crystals, which were synthesized at 12 GPa, 1473–1673 K. The modes at 3612, 3578, 3566, 3551 cm^{−1} show comparable negative temperature dependence, and the magnitude of $(\partial v_i / \partial T)_P$ decreases dramatically with frequency increasing. Whereas, the peak at 3477 cm^{−1}, which is attributed to protonation along the O1...O2 edge on the Si tetrahedron, has a positive temperature dependence. The absorbance intensities of all these OH bands remained almost the same when quenched to room temperature. On the other hand, we also evaluate the hydration effect on the thermodynamic properties (heat capacities). For the anhydrous forsterite sample, the intrinsic anharmonicity could significantly increase the heat capacity by 5~6% when extrapolated to 2000 K. Hydration further increase such difference to ~9%, in both the cases of M-substitution or Si-substitution. Hence, hydration in olivine has significant impact on the anharmonic contribution to the thermodynamic properties, as well as Equations of State and equilibrium isotope fractionation β -factor at high- P, T conditions in the deep mantle.

Keywords: forsterite; high-temperature FTIR; polarization of OH band; anharmonic contribution; thermodynamic properties; hydration mechanism

1. Introduction

Water is incorporated into many nominally anhydrous minerals (NAMs) in the form of hydrogen (H) point defects inside the crystal structures, which is fundamental to our understanding of water cycling in the deep Earth. Olivine, which constitutes ~50–60 vol. % of the upper mantle above the 410-km discontinuity, can take up significant water (hydroxyl groups) inside the lattice, as much as a few thousand ppmw (e.g., [1–7]). On the other hand, the presence of water inside the crystal structure can dramatically affect the physical and chemical properties of olivine, such as thermal and electrical conductivity [8,9], deformation [10], diffusivity [11–15], elastic properties [16].

Many experimental and theoretical studies have been reported exploring the hydrogen substitution mechanisms: (1) Mg²⁺/Fe²⁺ vacancies [1,2,6,13–26], which is the most common substitution in many hydrous silicate minerals; (2) Si⁴⁺ vacancies [27–35]; (3) combinations of Mg²⁺, Si⁴⁺, Ti⁴⁺, with M³⁺ vacancies [28,29,31,36–43]. In addition, another hydration mechanism with F-substitution is also proposed in both Fe-free and Fe-bearing olivine [44].

It is clear that the pressure conditions for the formation of hydrous olivine will have significant impact on the H substitution mechanisms. Taking the composition of Mg_2SiO_4 (forsterite) for example, if the hydrous forsterite were synthesized at the pressure conditions below 3 GPa (less than 100 km depth in the deep Earth), some strong OH stretching modes were observed in the low frequency range of $3000\text{--}3450\text{ cm}^{-1}$ by FTIR measurements [4,20,28,36,45–48]. While for the samples synthesized at pressures greater than 12 GPa (~350 km depth), the OH bands were only detected in the frequency range above 3450 cm^{-1} [1,2,7,23,49].

On the other side, it should be noted that the intrinsic anharmonicity (which will be described in more details in the following discussion, Section 3.4) plays an important role in simulating the thermodynamic properties of minerals at the high-temperature conditions of the deep mantle, such as heat capacities [50,51], P - V - T Equations of State [52,53], equilibrium isotope fractionation at high- P , T condition [54,55], etc. Gillet et al. [50] revealed that the anharmonic contribution to the heat capacity of anhydrous forsterite could be as large as 5.5% at 2000 K, while Qin et al. [33] and Marcondes et al. [56] also pointed out the anharmonic effects might be even more important when weak bonds (such as H bond) are involved.

In this study, we carried out high-temperature unpolarized and polarized FTIR measurements on the hydrous forsterite samples from Smyth et al. [2] ($\text{C}_{\text{H}_2\text{O}} = 3400\text{--}5000\text{ ppmw}$), and have more tight constraints on the temperature-dependence of the OH vibrational bands. Combining with the previous high-pressure and high-temperature Raman experiments on the hydrous forsterite samples [24,57], we will provide a detailed analyses of hydration effect on the anharmonic correction to the thermodynamic properties (such as heat capacities) of forsterite, in both the cases of M-substitution and Si-substitution, which should be significant and important for modeling the thermodynamics in the upper mantle.

2. Materials and Methods

2.1. Sample Preparation

In this experiment, we selected three simple crystal samples of hydrous forsterite with double-sided polishing: an unoriented crystal called Fo-unoriented (SZ0409B, $40 \times 100 \times 13\text{ }\mu\text{m}^3$, $d = 13\text{ }\mu\text{m}$), while two oriented samples named Fo001 (SZ0501B, $80 \times 70 \times 16\text{ }\mu\text{m}^3$) and Fo010 (SZ0410B, $70 \times 90 \times 11\text{ }\mu\text{m}^3$) in the directions of (001) and (010), respectively. These hydrous samples were synthesized at 12 GPa in the 5000-ton multi-anvil press apparatus at Bayerisches Geoinstitut [2], and the experimental temperatures are 1673 K and 1473 K for the oriented and unoriented ones, respectively. Based on the updated calibration from Withers et al. [58], the estimated water contents for these hydrous forsterite samples are about $3987 \pm 171\text{ ppmw}$ for the unoriented piece, while 3451 ± 348 and $4665 \pm 474\text{ ppmw}$ for the Fo001 and Fo010 samples, respectively.

2.2. FTIR at High Temperature

FTIR experiments were carried out on a Nicolet 5700 FTIR spectrometer at the State Key Laboratory of Geological Processes and Mineral Resources, China University of Geosciences (Wuhan). The spectrometer was equipped with a Continuum microscope, a KBr beam splitter and a liquid-nitrogen-cooled MCT-A detector. A wire grid IR polarizer was applied to obtain polarized spectra. For the high-temperature IR absorption experiments, an external Linkam FTIR1500 heating stage with windows of sapphire slices. The heating stage was placed on the sample stage of the microscope and the sample chamber inside was filled with N_2 as a protecting gas at high temperatures. During the measurements, high temperatures were achieved by a resistance heater inside the heating stage and measured by an automatic temperature control unit (a Linkam TMS94) which could be programmed with the accuracy of $0.1\text{ }^\circ\text{C}$. Spectrum was recorded in the wavenumber range of $3000\text{--}4000\text{ cm}^{-1}$ by 256 scans, with a resolution of 4 cm^{-1} .

We collected both unpolarized and polarized FTIR spectra on the two oriented crystal pieces, as well as unpolarized spectra on the Fo-unoriented, in the temperature range from 293 K to 1243 K with an increment of 50 K. At each target temperature, temperature was maintained for at least 5 min before measurement for thermal equilibrium inside the sample chamber. To analyze temperature dependence of each OH band in the samples, Peakfit v4.12 software was adopted [41,51].

3. Results and Discussion

3.1. Polarized FTIR Spectra at Ambient Temperature

The unpolarized FTIR spectra of these hydrous forsterite samples at ambient condition are presented in Figure 1, with the OH bands distributed in the frequency range of 3450–3620 cm^{-1} . Peaks at 3612, 3578, 3566, 3552, and 3477 cm^{-1} are well resolved for the Fo-unoriented sample, while the extra peak at 3542 cm^{-1} could be further identified in the Fo010. We also collected polarized FTIR spectra of oriented Fo001 and Fo010 samples at room temperature (Figure 2a,b), in a rotation range from 0 to 180° with an interval of 15°. We selected the a-axis as the polarization angle of 90°, and consequently the c and b axes were aligned in the direction of 0° (or 180°) for the Fo001 and Fo010 samples, respectively. Variation of the integrated absorbance for these OH bands with the rotation angle could be clearly resolved for the OH bands at 3612, 3578, 3566, 3551, and 3477 cm^{-1} (Figure 3a,b).

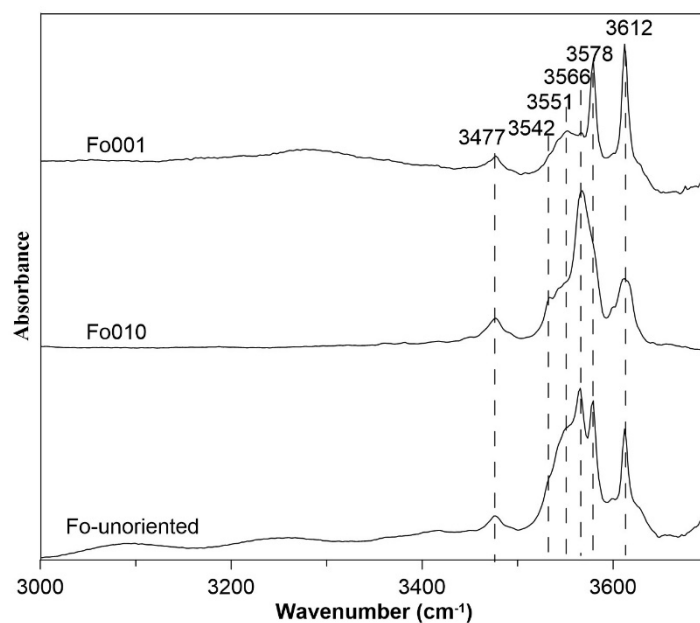


Figure 1. The unpolarized Fourier Transform infrared (FTIR) spectra measured for the hydrous forsterite samples at ambient condition, with the peak positions labeled.

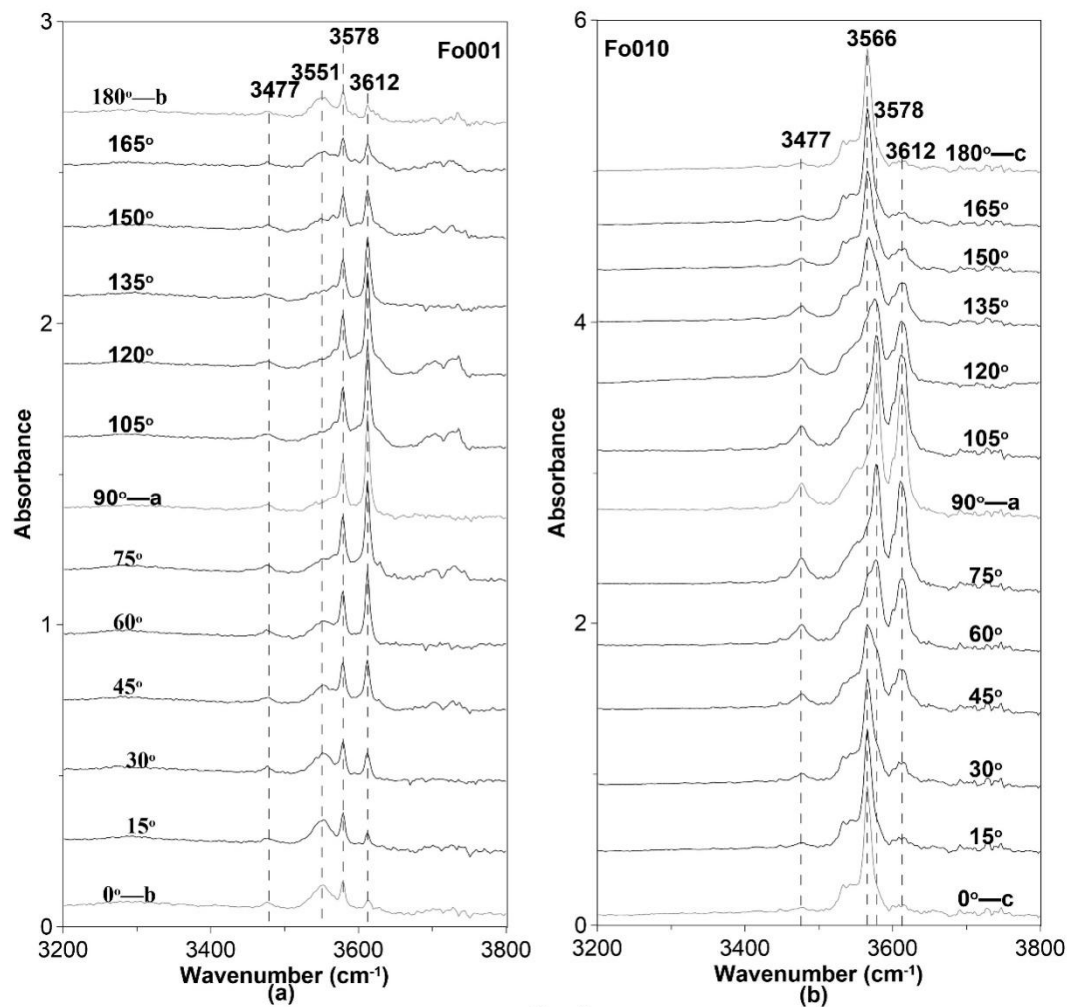


Figure 2. The polarized transmission FTIR spectra for the oriented Fo001 (a) and Fo010 (b) samples with an interval of 15° for the measurements. The angle of 90° is selected along *a* axis, and consequently the direction for 0° (180°) is aligned along *b* and *c* axes for the pieces of (001) and (010), respectively.

The $E//a$ spectra show strong absorption for the OH bands at 3612 and 3578 cm^{-1} for Fo001 and Fo010 samples. The peaks at 3566 and 3551 cm^{-1} show minimum absorptions with $E//a$, while maximum absorptions with $E//c$ (Figure 3a) and $E//b$ (Figure 3b), respectively. The polarized spectra of Fo010 show the strongest absorption for band at 3477 cm^{-1} with $E//a$, with respect to $E//c$. These results are generally consistent with the earlier polarized FTIR measurements [2,4,23,36]. Hence, the polarization phenomena for the OH bands are nearly independent with the water concentration inside the crystal structure.

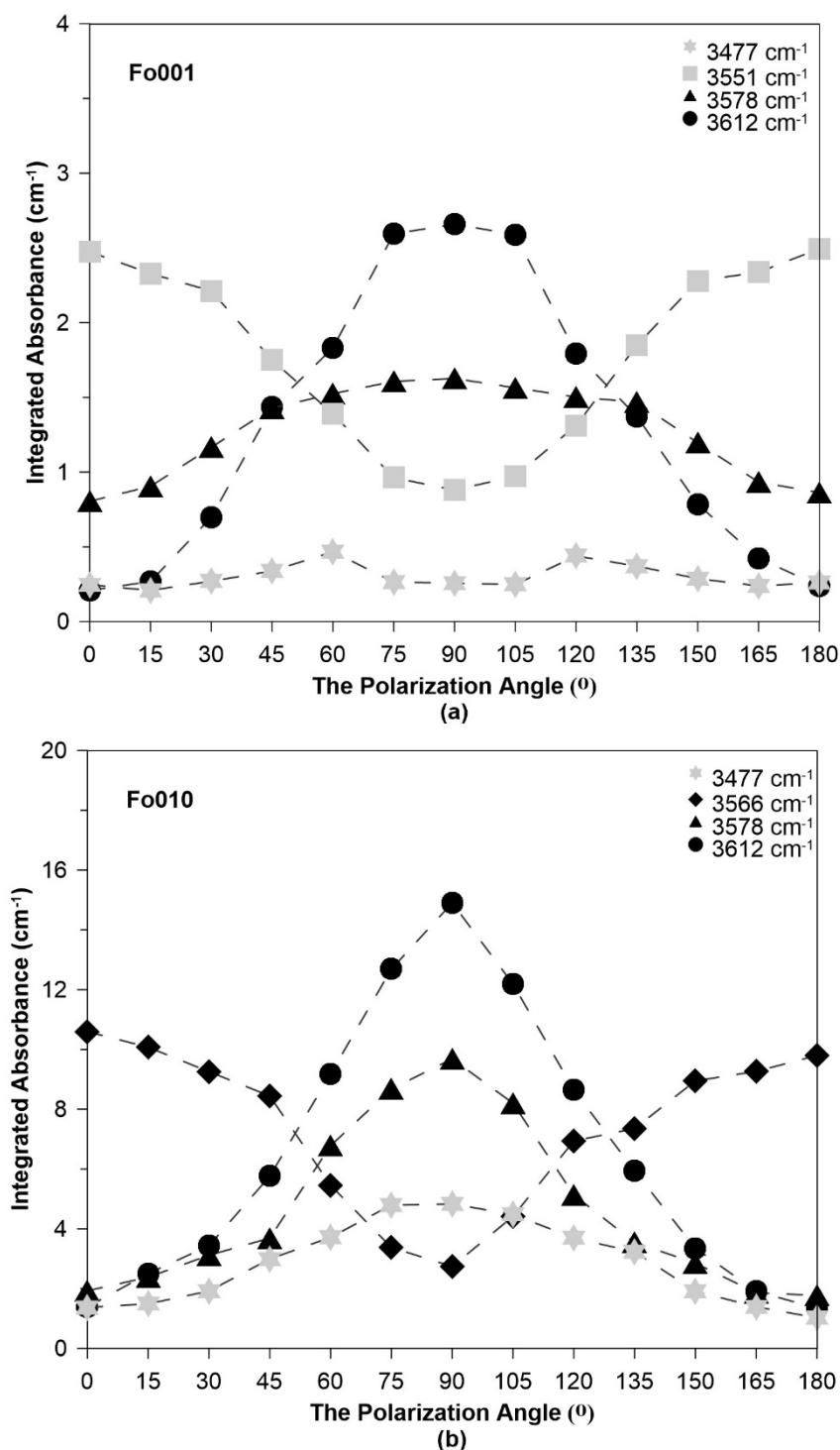


Figure 3. Variation of the integrated absorbances of the OH bands with the polarization angle for the oriented Fo001 (a) and Fo010 (b) samples. The angle of 90° is selected along *a* axis.

3.2. Hydrogen Substitution Mechanism

There has been a long debate on the hydration mechanism in Mg-pure forsterite and Fe-bearing olivine: M-substitution ($\text{Mg}^{2+} = 2\text{H}^+$) [1,2,6,13–15,17–24], and Si-substitution ($\text{Si}^{4+} = 4\text{H}^+$) [27–34,36,41]. The polarized FTIR spectra in this study could provide an experimental check for the hydration positions inside the crystal structure for either case of M-substitution or Si-substitution.

The OH stretching vibrations at 3612 cm^{-1} , with a calculated O...O bond length ($d_{\text{O}\cdots\text{O}}$) of 3.05 \AA [59], is strongly polarized along a axis. Mg substitution mechanism has proposed that the most likely attribution of this OH band is the O3...O3 edge ($d_{\text{O3}\cdots\text{O3}} = 2.99\text{ \AA}$ as refined from Hushur et al., [24]) in the M2 octahedron [2] (Figure 4a). While others [24,49] attribute it to the O1...O2 edge shared between M1 octahedra but with a short length of 2.85 \AA , our polarized FTIR spectra support such site should be more proper for the band at 3578 cm^{-1} in the following discussion. On the other side, Lemaire et al. [36] associated this band with a O–H bond toward Si vacancy along O1–V_{Si} (Figure 4c) perfectly in the a direction. Meanwhile, the theoretical calculations [30–33] attribute it to protonation along the O1...O2 edge in SiO₄ tetrahedron, which deflects away from the a axis with an intersection angle $\sim 31^\circ$.

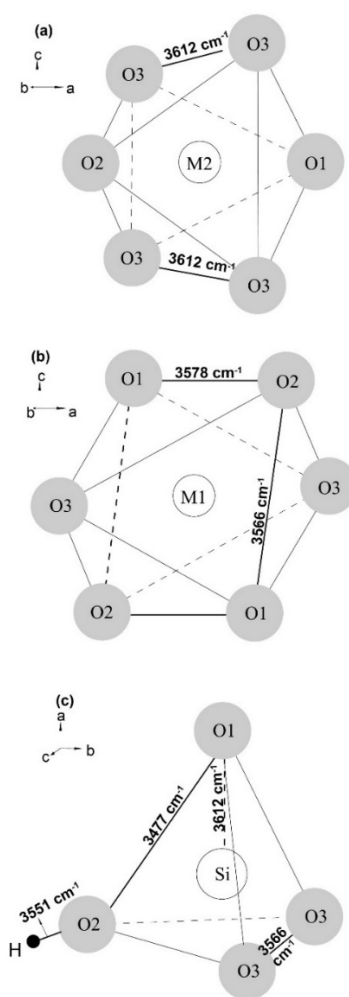


Figure 4. Sketch of (a) M2 octahedron, (b) M1 octahedron and (c) Si tetrahedron for forsterite, based on the single-crystal structure refinement from Hushur et al. [24]. The potential attributions for the OH bands in both the cases of M-substitution and Si-substitution are marked, which are in agreement with this polarized FTIR measurement.

The OH band at 3578 cm^{-1} is also polarized along the a axis at a lower frequency (a shorter O...O edge) as compared with the one at 3612 cm^{-1} . The peak of 3578 cm^{-1} used to be attributed to H located along the unshared O1–O2 (2.85 Å) edge of the M1 octahedron [2,16] (Figure 4b). The studies supporting Si-substitution assign this band to protonation along the O1...O2 edge (2.75 Å) [36] or along the O1...O3 edge (2.76 Å) of Si tetrahedron [30–33]. However, the orientations of these edges mismatch with the a axis with intersection angles of more than 30° .

The OH band at 3566 cm^{-1} shows strong polarization along c axis with a calculated $d_{\text{O...O}}$ of 3.06 Å [60]. It has been attributed to the unshared O1–O2 edge with a measured $d_{\text{O...O}}$ of 3.02 Å on the M1 octahedron (Figure 4b) [2] and the protonation along the O3...O3 edge of the Si tetrahedron [36], with a little shorter O...O bond length (2.59 Å) (Figure 4c). Both of these assignments are in agreement with the polarization observed in this study. While the theoretical calculations [30–33] prefer to ascribe this OH band to another O1...O3 edge on the Si tetrahedron ($d_{\text{O1...O3}} = 2.85\text{ Å}$), which show an intersection angle as large as 62° with respect to the c axis.

The OH band at 3551 cm^{-1} is polarized along b axis and proposed as one of the protons around the O2 anion, pointing away from the Si tetrahedral center and located in an adjacent interstitial site (Figure 4c) [19,32,33,47]. In addition, Balan et al. [61] proposed that the broad band around 3551 cm^{-1} may be due to a (charged) interstitial OH group next to a five-coordinated Si, which was later contested by Xue et al. [32], since such ^{29}Si NMR peak was not observed. While Yang et al. [34] ascribed this OH-stretching mode to the O1...O3 edge on the Si tetrahedron on the basis of its temperature dependence, this needs further checking considering its polarization.

Finally, the peak at 3477 cm^{-1} shows most absorption with an intersection angle of $\sim 30^\circ$ to a axis (or 60° to b axis) in (001) plane (Figure 3a), while least absorption along c axis in (010) plane (Figure 3b). Such polarization matches very well with the orientation of the O1...O2 edge on the Si tetrahedron [24], which is perpendicular to c axis, and with an intersection angle of 32.5° to a axis, which is also supported by Yang et al. [34]. Hence, from this polarized FTIR measurement, we proposed the OH band at 3477 cm^{-1} should be a more proper candidate for the protonation along O1...O2 edge on the SiO_4 tetrahedron, compared with the ones at 3578 and 3612 cm^{-1} .

3.3. FTIR Spectroscopy at High Temperature

We collected in situ unpolarized FTIR spectra from 293 K up to 1243 K for both the unoriented (Figure 5a) and oriented crystals Fo001 (Figure 5b) and Fo010 (Figure 5c) directions, as well as polarized FTIR spectra at elevated temperatures for the oriented pieces Fo001 (Figure 6a,b) and Fo010 (Figure 6c,d). When each sample was quenched to room temperature from the highest temperature, additional FTIR spectra were also measured, and compared in these figures. There are no significant differences for the absorbances of these OH bands before and after heating, indicating little dehydration for hydrous forsterite in the heating process up to $\sim 1300\text{ K}$, which was also observed by Yang et al. [34,57]. Generally, the peaks become weaker and boarder at higher temperatures in FTIR spectra. In our measurement, the OH bands at 3612 , 3578 , 3566 , 3551 cm^{-1} were always observed up to 1243 K, while the one at 3477 cm^{-1} could only be detected up to $\sim 700\text{ K}$ due to small intensities in FTIR (Figure 5a,c; Figure 6c,d). All these OH bands turned back with similar intensities when quenched to room temperature from the high temperature of 1243 K (Figure 5a,c; Figure 6c,d). It should be noted that our whole heating procedure was fulfilled within 1.5 h, and little dehydration occurred due to the relatively low H diffusion rate below 1373 K in hydrous forsterite [35]. On the other hand, Koch-Müller et al. [62] reported significant dehydration in hydrous forsterite with the heating duration as long as 240 h, although the experimental temperatures were still limited below 1273 K.

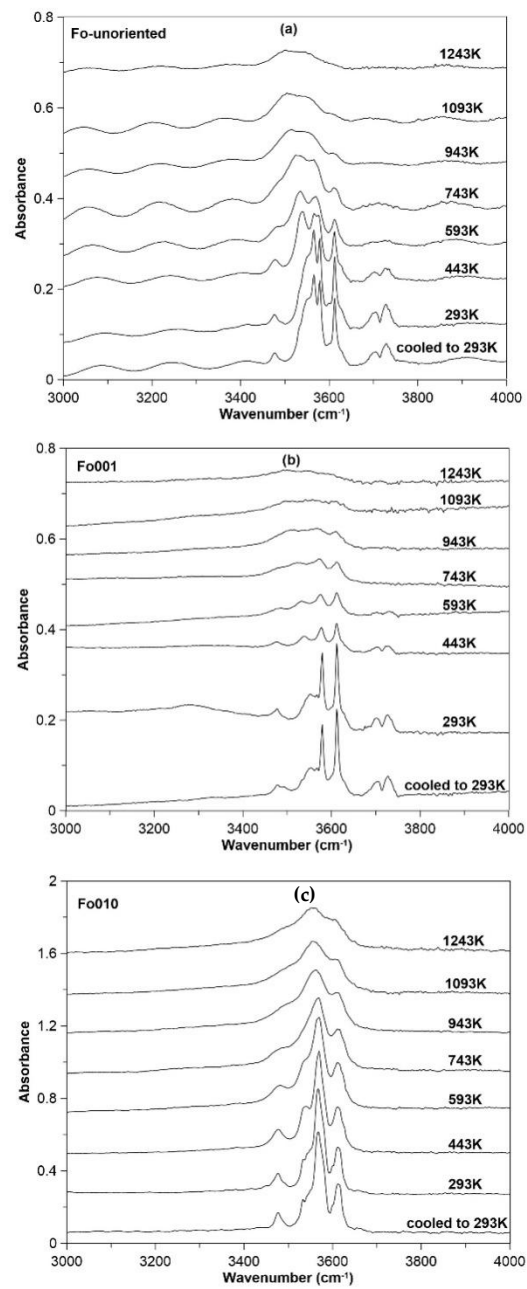


Figure 5. Selected unpolarized IR spectra for the Fo-unoriented (a), oriented Fo001 (b) and Fo010 (c) samples at elevated temperatures.

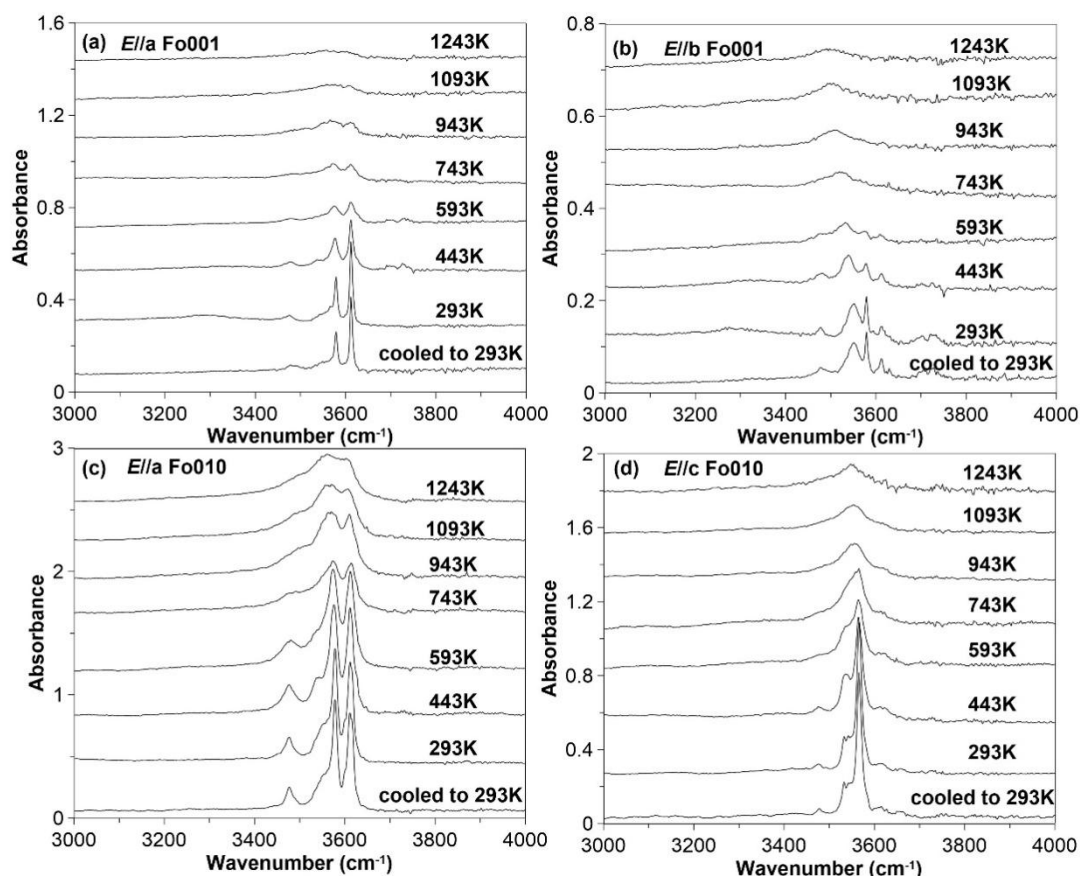


Figure 6. Polarized IR spectra for the oriented Fo001 (a for $E//a$ and b for $E//b$) and Fo010 (c for $E//a$ and d for $E//c$) directions, at high temperatures.

The positions of these OH bands at elevated temperatures were fitted from both the oriented and unoriented FTIR spectra, and the variation of the frequencies with temperature is plotted for the oriented pieces in the directions of (001) (Figure 7a) and (010) (Figure 7b), as well as the unoriented one (Figure 7c). The neighboring peaks at 3578 and 3566 cm^{-1} overlap severely in the unpolarized FTIR spectra, especially at temperatures above 450 K, but could be well resolved in the polarized spectra, since these two bands are polarized in different directions along a and c axes, respectively. Linear regressions between frequencies and temperature are fitted to all these OH bands, and the slopes of $(\partial v_i / \partial T)_p$ are summarized in Table 1. The OH bands at 3612, 3578, 3566, and 3551 cm^{-1} have negative temperature-dependences (Figure 8), which is consistent with the general trend from the previous studies [34,41]. Yang et al. [34] conducted the high- T measurement on one unoriented crystal piece, while Yang et al. [41] measured the high- T polarized FTIR on a Fe-bearing San Carlos olivine sample with a water content less than 300 ppmw. The magnitudes of dv_i/dT decrease from 0.056 $(\text{cm} \cdot \text{K})^{-1}$ at 3551 cm^{-1} to less than 0.01 $(\text{cm} \cdot \text{K})^{-1}$ at 3612 cm^{-1} , and weaker OH bands (at higher frequencies) are less sensitive to temperature variation. Besides, the peak at 3477 cm^{-1} shows a positive temperature-dependence of +0.016~+0.027 $(\text{cm} \cdot \text{K})^{-1}$, and the previous measurements [34,41] also reported a temperature-dependence range of −0.0043~+0.024 $(\text{cm} \cdot \text{K})^{-1}$ for the OH bands in the range of 3400~3500 cm^{-1} . In addition, our high- T FTIR experiment is also consistent with the low- T results from Ingrin et al. [47]: The band at 3566 cm^{-1} (measured at 79 K, which shifted to 3551 cm^{-1} at room temperature) shows a negative temperature-dependence in larger magnitude as compared with the ones at higher frequencies, and this mode is also attributed to the interstitial H position by [47]. As temperature increases, the covalent bond between O2 and the interstitial H becomes weaker, and the OH band at 3551 cm^{-1} shifts to lower frequency quickly. Consequently, the neighboring OH bond

along the O1–O2 edge of the Si tetrahedron gets strengthened, as indicated by ‘blue-shift’ of the mode at 3477 cm^{-1} at elevated temperatures.

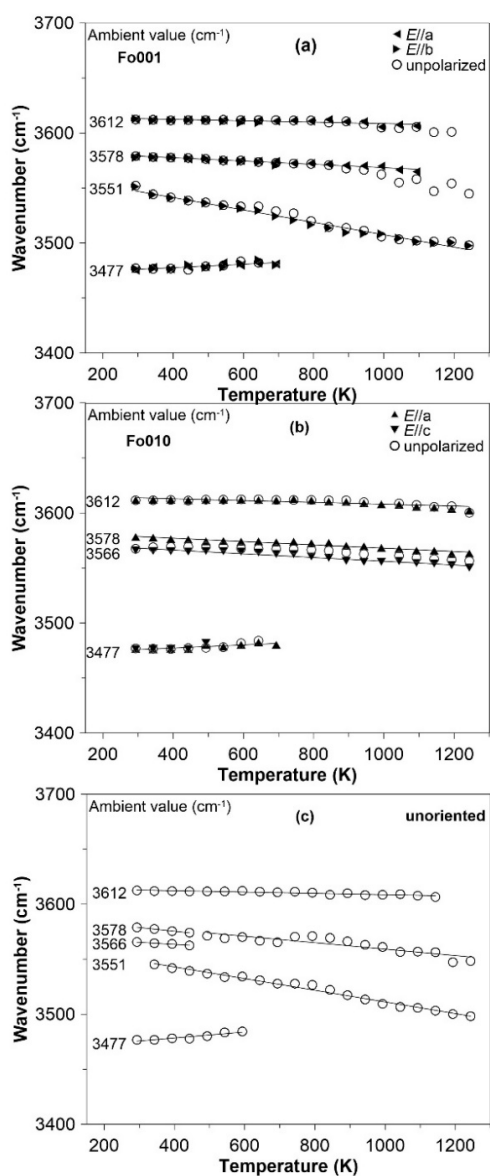


Figure 7. Variation of the frequencies for the OH bands with temperature for the oriented Fo001 (a) and Fo010 (b) samples, as well as the Fo-unoriented (c). Linear regressions (solid lines) are fitted for the datasets and the frequencies of at room temperatures are also listed in the figures.

Table 1. The main OH bands with the temperature dependence $(\partial v_i / \partial T)_P$ for the oriented and unoriented pieces of hydrous forsterite.

OH-Band (cm^{-1})	$(\partial v_i / \partial T)_P$ ($\text{cm} \cdot \text{K}^{-1}$)		
	Fo001	Fo010	Fo-Unoriented
3612	−0.008(6)	−0.009(4)	−0.006(1)
3578	−0.016(2)	−0.015(2)	−0.021(5)
3566		−0.016(8)	−0.018(8)
3551	−0.056(4)		−0.053(7)
3477	0.016(1)	0.018(2)	0.027(2)

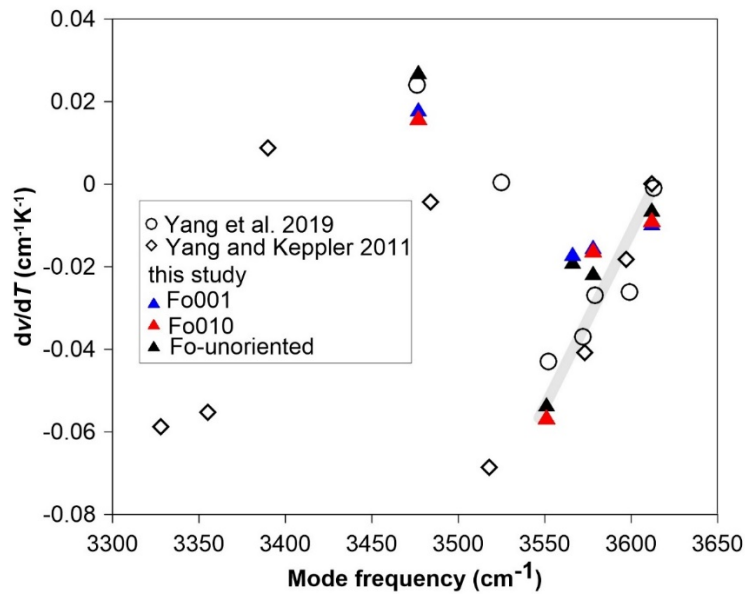


Figure 8. Comparison of the temperature-dependence for the frequencies of OH bands of hydrous olivine ([34,41]; this study).

3.4. Hydration Effect on the Intrinsic Anharmonicity

In this section, we will take a further step to check hydration effect on the thermodynamic properties (heat capacities), on the basis of this high- T FTIR measurement for the OH bands, together with the Raman experiments on the lattice vibrations of hydrous forsterite samples at high- P and high- T conditions [24,57]. The thermodynamic properties (such as internal energy, heat capacities, as well as isotope fractionation) of silicate minerals at high- P , T conditions generally simulated with the Debye model, which only considers the harmonic lattice vibrations (e.g., [63,64]). On the other hand, the anharmonic contribution become severe at mantle temperatures, and cannot be ignored [33]. For example, the volume of materials should have been independent from temperature if the atoms inside the crystal structures only behave harmonic vibration. In fact, the general behavior of thermal expansion at high temperatures is one aspect of anharmonicity (external anharmonicity). Additionally, Gillet et al. [50] revealed that the intrinsic anharmonic contribution to the modeled isochoric heat capacity (C_V) could be as large as 5.5% for anhydrous forsterite. In this study, we would take a further step to evaluate the hydration effect on the contribution of intrinsic anharmonicity to the thermodynamics in forsterite.

The contribution of the temperature- and pressure-factors to the vibrational frequency (ν_i) can be divided into two parts: pure volume variation at high P, T conditions (external anharmonicity) and pure P - T contribution from intrinsic anharmonicity [50,57,65]. The Grüneisen parameters in isobaric (γ_{iP}) and isothermal (γ_{iT}) modes, as well as the intrinsic anharmonicity (a_i), are derived in Equations (1)–(3):

$$\gamma_{iP} = \left(\frac{\partial \ln \nu_i}{\partial \rho} \right)_P = -\frac{1}{\alpha \nu_{0i}} \left(\frac{\partial \nu_i}{\partial T} \right)_P \quad (1)$$

$$\gamma_{iT} = \left(\frac{\partial \ln \nu_i}{\partial \rho} \right)_T = \frac{K_T}{\nu_{0i}} \left(\frac{\partial \nu_i}{\partial P} \right)_T \quad (2)$$

$$a_i = \left(\frac{\partial \ln \nu_i}{\partial T} \right)_V = -\alpha (\gamma_{iP} - \gamma_{iT}) \quad (3)$$

where ν_{0i} are the mode frequency at ambient environment, while $(\partial \nu_i / \partial T)_P$ and $(\partial \nu_i / \partial P)_T$ are the temperature and pressure derivatives of the frequency (ν_i), respectively. α is the mean thermal expansion coefficient ($38.1 \times 10^{-5} \text{ K}^{-1}$ from Ye et al. [5]), and K_T is the isothermal bulk modulus

(121.6 GPa from Manghnani et al. [16]) at ambient condition. Hushur et al. [24] and Yang et al. [57] conducted high-pressure and high-temperature Raman measurements on this hydrous forsterite sample, while we carried out high-temperature FTIR measurement in this study. Calculated isobaric (γ_{iP}) and isothermal (γ_{iT}) Grüneisen parameters, as well as the intrinsic anharmonic parameters for the hydrous forsterite (Supplementary Table S1), as compared with those for anhydrous forsterite [50], are shown on the Figure 9a–c. The magnitudes of the Grüneisen parameters (γ_{iP} and γ_{iT}) for OH-stretching modes (typically less than 0.15) are significantly smaller than those for the lattice vibrations. Then, the corresponding a_i parameters for OH-stretching bands are in the value range of $-1 \sim 0$ (10^{-5} K^{-1}), which are comparable to those for the internal vibrational modes in SiO_4 tetrahedron ($400 \sim 1000 \text{ cm}^{-1}$, including both bending and stretching), while the external lattice vibrations (below 400 cm^{-1}) yield negative a_i parameters with significantly larger magnitudes.

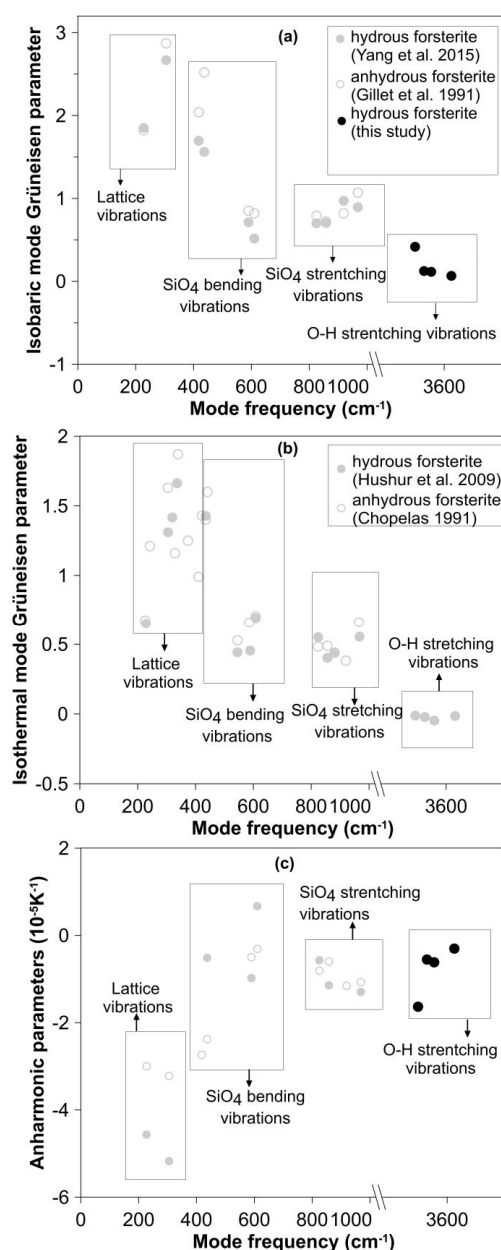


Figure 9. The isobaric (a), isothermal (b) mode Grüneisen parameters and intrinsic anharmonic parameters (c) for the anhydrous [50,66] and hydrous forsterite, calculated from the Raman measurements at high temperature (this study and Yang et al. [57]) and high pressure [24].

The space group of olivine is *Pbnm*, and in the unit cell (Mg_2SiO_4 , $Z = 4$), there are 8 Mg atoms (in two different octahedral sites M1 and M2), 4 Si (in a single tetrahedral site), as well 16 O atoms (classified as O1, O2, O3). In total, there are totally 84 vibrational modes in the crystal structure, with 3 acoustic ones, as well as 81 optical ones, which could be detected by Raman or IR spectrum. Different modes have been proposed to classify these optical (lattice) modes in different frequency ranges, such as Model 1 [67] and Model 2 [50] shown in Figure 10a,b, respectively. In Model 1, the transitions of SiO_4 tetrahedron T(Si) (external modes) is classified in a separated continuum (105–227 cm^{-1}) away from the external modes of T(M) (transitions of MO_6 octahedra) and R(Si) (Rotations of SiO_4), as well as v_2 (symmetric bending modes inside SiO_4); while all these modes are combined in the same continuum (105–482 cm^{-1}) in Model 2. The asymmetric bending mode v_4 is denoted in the continuum of 505–644 cm^{-1} , and the internal stretching modes inside SiO_4 of v_1 (symmetric) and v_3 (asymmetric) are distributed in another continuum with higher frequency (825–964 cm^{-1}). Although it is impossible to detect all these optical modes in the high- P,T Raman and FTIR measurements, we adopted the measured mean intrinsic anharmonic parameters (a_i) as the average value for the whole set of spectroscopic modes in a continua, and the averaged a_i parameters in different continua are compared between both the hydrous and anhydrous samples.

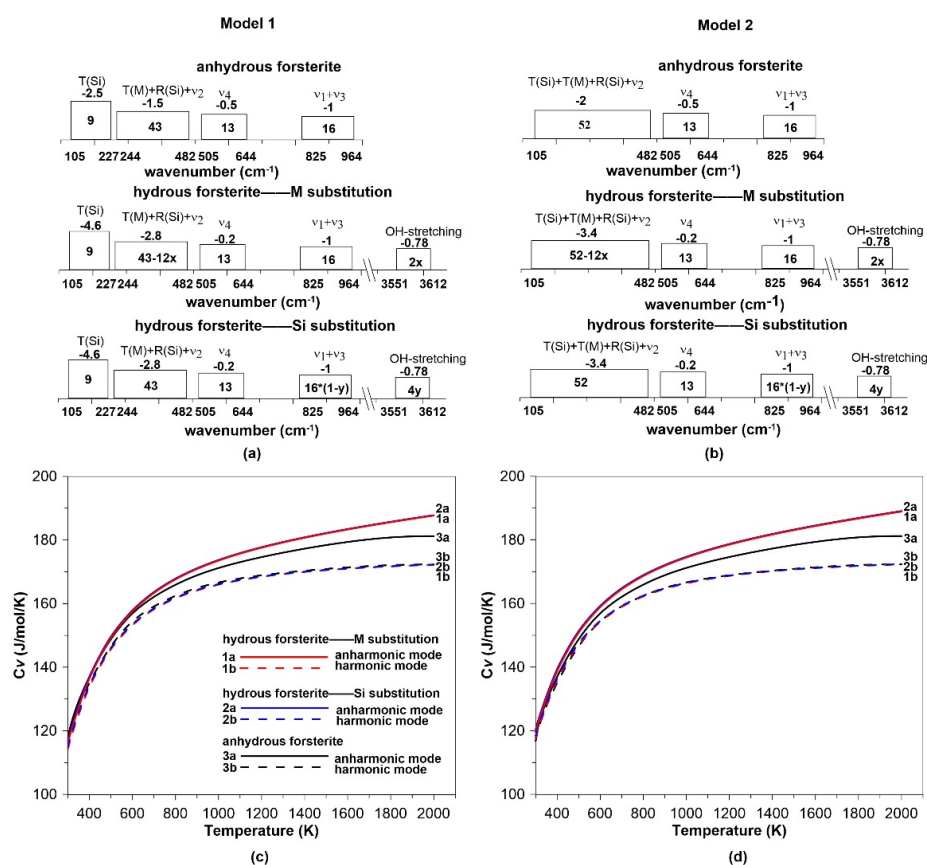


Figure 10. Modes of density of states for anhydrous and hydrous forsterite from (a) Model 1 [67] and (b) Model 2 [50]. The formula is $\text{Mg}_{2-x}\text{H}_{0.138}\text{SiO}_4$ ($x = 0.0686$) and $\text{Mg}_2\text{H}_{0.138}\text{Si}_{1-y}\text{O}_4$ ($y = 0.0345$) assuming all OH with M-substitution and Si-substitution, respectively. The values $x = 0.0686$ and $y = 0.0345$. The boxes denote the continua for different groups of optical modes. The upper and lower cutoff frequencies for each continuum are also labeled below the box. The numbers inside and above each box represent the number of modes and the mean (a_i) parameter for the vibrational modes in each continuum (Figure 9 and Supplementary Table S1), respectively. Comparisons for the isochoric heat capacities, C_v , for anhydrous and hydrous forsterite samples are made in (c) (Model 1) and (d) (Model 2).

In this discussion, we firstly considered either M-substitution ($\text{Mg}^{2+} = 2\text{H}^+$) or Si-substitution ($\text{Si}^{4+} = 4\text{H}^+$), in the extreme condition of OH-saturation in forsterite ($\text{C}_{\text{H}_2\text{O}} = 8900$ ppmw.) [2,5]. For the case of M-substitution, the chemical formula for this hydrous forsterite can be expressed as $\text{Mg}_{1.931}\text{H}_{0.138}\text{SiO}_4$, by assuming all OH with M-substitution ($x = 0.0686$ in Figure 10a,b). The number of OH-stretching modes in the continuum ($3551\text{--}3612\text{ cm}^{-1}$) is $2x$. On the other side, there are 24 modes associated with the transitions of MO_6 octahedra, and hence, the number of $12x$ should be subtracted for the T(M) modes. While in the case of Si-substitution, the formula would be changed to $\text{Mg}_2\text{Si}_{0.965}\text{H}_{0.138}\text{O}_4$, with a vacancy of 3.45% in Si sites ($y = 0.0345$ as in Figure 10a,b). To simplify the calculation, we assume that Si-substitution only affects the internal Si–O stretching modes, and then the number of $v_1 + v_3$ modes is decreased to $16 \cdot (1-y)$, with a number of $4y$ for the OH-stretching modes.

According to the models from Kieffer [68] and Gillet et al. [50], the contribution to isochoric heat capacity (C_V) from a set of m optic continua from various types of spectroscopic modes is given as:

$$C_v = 3nR \sum_{i=1}^m \frac{n_i}{N} \int_{v_{li}}^{v_{ui}} \frac{z^2 \exp(z) dz}{(v_{ui} - v_{li}) [\exp(z) - 1]^2} = 3nR \sum_{i=1}^m C_{vi}^h \quad (4)$$

where $z = (h_i/k_B T)$ inside the integration, n is the number of atoms in the mineral's structural formula; R is the gas constant, n_i is the number of modes in the continuum, N is the total number of vibrational modes, and ui and li are the lower and upper cutoff frequencies of continuum, respectively. When the intrinsic anharmonicity is taken into consideration, the isochoric heat capacity (C_V) could be revised as (e.g., [50]):

$$C_v = 3nR \sum_{i=1}^m C_{vi}^h (1 - 2a_i T) \quad (5)$$

where C_{vi}^h is the harmonic part of the heat capacity.

The molar isochoric heat capacities (C_V) are calculated as a function temperature for both anhydrous and hydrous forsterite samples in Models 1 (Figure 10c) and 2 (Figure 10d). For each sample, the heat capacities are calculated in both harmonic and anharmonic cases, on the basis of Equations (4) and (5), respectively. Both M-substitution (red color) and Si-substitution (blue color) are considered for the hydrous sample. There is no significant difference between the anhydrous and hydrous samples in the harmonic approximation. Nevertheless, the anharmonic contribution increases the heat capacity (C_V) of anhydrous forsterite by 5.1% (in model 1) or 5.7% (in Model 2), when extrapolated to 2000 K [50], while hydration further increases such difference up to 9% (in Model 1) or 9.5% (in Model 2) for both the cases of M-substitution and Si-substitution. Hence, hydration could significantly increase the anharmonic contribution to the thermodynamic properties of forsterite, which is independent of M-substitution or Si-substitution.

Next, we evaluate the isobaric heat capacity (C_P) for both the anhydrous and hydrous samples (in Model 1), on basis of Equation (6), and select M-substitution as representative for the hydrous case (Figure 11). The anharmonic contribution to isobaric heat capacity is 4.7% and 8.1% for anhydrous and hydrous forsterite, respectively, at 2000 K.

$$C_P = C_v + T \cdot V \cdot \alpha^2 \cdot K_T \quad (6)$$

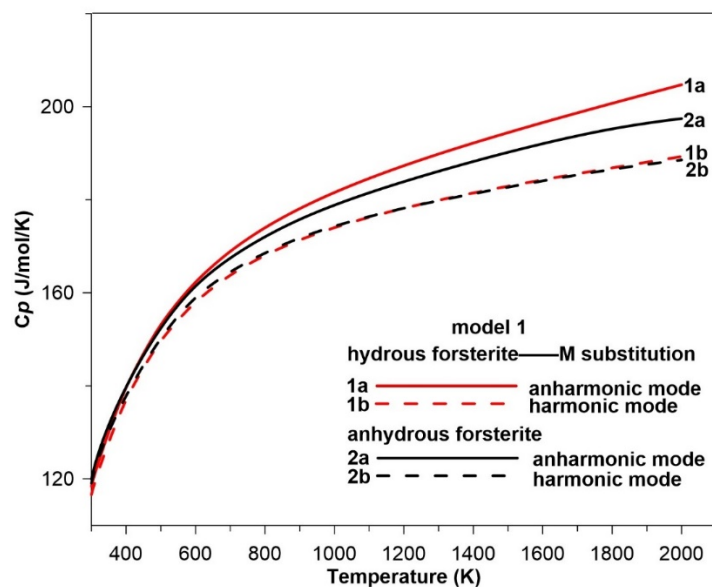


Figure 11. Comparison of the isobaric heat capacities for both the anhydrous and hydrous forsterite samples.

On the other hand, we simulate the C_V profile for hydrous forsterite sample with 4500 ppmw. H_2O . In this case, $x = 0.0343$ and $y = 0.0172$, and we select Model 1 as representative for both M-substitution and Si-substitution. The anharmonic contribution to C_V (difference between the calculations with anharmonic correction and in harmonic approximation) is plotted as a function of temperature in Figure 12. In the case of Si-substitution, the anharmonic correction to the heat capacity is 8.7% and 9.0% for the forsterite samples with 4500 ppmw and 8900 ppmw H_2O at 2000 K; while there is little difference between these hydrous samples for the case of M-substitution.

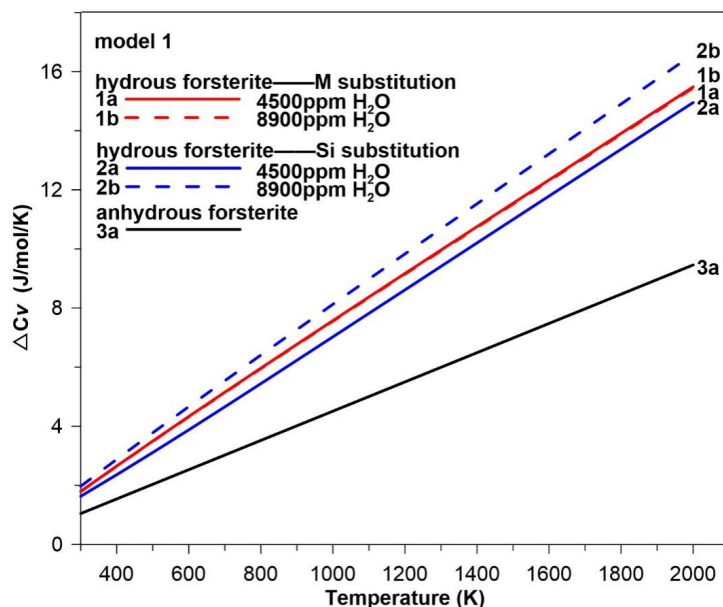


Figure 12. Comparison of the difference of isobaric heat capacities between the cases for harmonic approximation and with intrinsic anharmonic contribution for anhydrous and hydrous forsterite.

The contribution to the heat capacity from the OH-stretching modes themselves are tiny, due to the very few numbers for mode density of state and high frequencies. However, previous Raman

studies at high- P,T conditions [24,57] revealed that hydration substitution significantly affects the intrinsic anharmonic parameters (a_i) of the lattice vibrations ($<1000\text{ cm}^{-1}$), especially the external modes ($<450\text{ cm}^{-1}$), such as T(M), T(Si) and R(Si). Moreover, the modes at lower frequencies have larger weights in determining the heat capacity as a whole.

On the other hand, the modes at lower frequencies also play more important role in simulating the equilibrium traditional isotope fractionation (e.g., [54,55,69]). A widely accepted correlation between the pressure- and temperature-dependence of the reduced isotopic partition function ratio (β -factor) has been established as (e.g., [70]):

$$\left[\frac{\partial \ln}{\partial P} \right]_T = -\frac{\gamma \cdot T}{K_T} \cdot \left[\frac{\partial \ln}{\partial T} \right]_V \quad (7)$$

The Grüneisen parameter, is expressed in the cases of quasi-harmonic approximation (Equation (8)) and with intrinsic anharmonic correction (Equation (9)):

$$\gamma = \frac{\sum_i \gamma_i (u_i \cdot \coth(u_i/2) - u_i^* \cdot \coth(u_i^*/2))}{\sum_i (u_i \cdot \coth(u_i/2) - u_i^* \cdot \coth(u_i^*/2))} \quad (8)$$

$$\gamma = \frac{\sum_i \gamma_i (1 - a_i \cdot T) \cdot (u_i \cdot \coth(u_i/2) - u_i^* \cdot \coth(u_i^*/2))}{\sum_i (1 - a_i \cdot T) \cdot (u_i \cdot \coth(u_i/2) - u_i^* \cdot \coth(u_i^*/2))} \quad (9)$$

where the dimensionless frequency $u_i = h \cdot \nu_i / (k_B \cdot T)$, while i and a_i are the isothermal Grüneisen parameter and the intrinsic anharmonic parameter, respectively. * denotes for the heavier isotopes, which could be ^{26}Mg , ^{30}Si or ^{18}O in forsterite, and the frequency shifts of the vibrational modes (ν_i or u_i^*) can be calculated according to the isotopic mass effect (e.g., [71]). As shown in Figure 9, hydration in forsterite could significantly affect the a_i parameters, as well as the i parameters (no matter it is M-substitution or Si-substitution). Hence, hydration could have further impact on modeling the-factors for the traditional isotopes (Mg, Si and O) in olivine at the high- P,T conditions (Equation (8)), and the anharmonic correction is necessary for evaluating the pressure effect on the equilibrium isotope fractionations between minerals (Equation (9)) [70].

4. Conclusions

Polarized FTIR measurements were carried out on hydrous forsterite crystals. The polarizations of the OH bands at 3612, 3578, 3566, 3551, 3477 cm^{-1} are well constrained. In the case of M-substitution, the polarizations of the modes at 3612, 3578 and 3566 cm^{-1} match well with the protonation along the O3...O3 edge in M2 site, the unshared ($E//a$) and shared ($E//c$) O1...O2 edges in M1 site, respectively. In the case of Si-substitution, the polarizations of the OH bands at 3612 and 3551 cm^{-1} are in agreement with the orientations of O1- V_{Si} and O2-H pointing away from Si, while the ones at 3566 and 3477 cm^{-1} could be properly attributed to the O3...O3 and O1...O2 edges in SiO_4 tetrahedron, considering their polarizations.

High-temperature polarized FTIR experiment provides robust constraint on the temperature-dependence of the OH-stretching modes. In the frequency range above 3550 cm^{-1} , the frequency have negative temperature-dependence, with their magnitudes decrease rapidly with frequency increasing. While the OH bands in the range 3400–3500 cm^{-1} typically show positive temperature-dependence but with the magnitudes no more than 0.02 $\text{cm}^{-1}/\text{K}^{-1}$. Then the mode at 3477 cm^{-1} might be in a quite different crystal environment, compared with the other OH bands at higher frequencies in forsterite.

We simulate the heat capacities of hydrous forsterite, as a function of temperature. Hydration dramatically increases the intrinsic anharmonic contribution to the heat capacities for both M- and Si-substitutions, no matter which substitution mechanism is considered. This is consistent with the high-temperature X-ray diffraction that hydration also increase the thermal expansivity (external

anharmonicity) for forsterite, as well as its high-pressure polymorphs of wadsleyite and ringwoodite in the mantle transition zone (410–660 km) [5]. Although the contribution from the OH-stretching vibrations themselves is very small, by affecting the anharmonic parameters (a_i) of the lattice vibrations, especially the external modes in the frequency range below 500 cm^{-1} , hydration could make important impact on the thermodynamic properties of olivine, such as internal energy, entropy, heat capacities, as well as isotope fractionation (Mg, O, or Si) at the high- P,T conditions in the upper mantle.

Supplementary Materials: The following are available online at <http://www.mdpi.com/2075-163X/9/9/512/s1>, Table S1: The Raman shifts and OH bands by FTIR (ν_i), temperature dependence of ν_i ($\partial\nu_i/\partial T$)_P, isobaric mode Grüneisen parameters, as well as intrinsic anharmonic parameters (a_i) for hydrous forsterite.

Author Contributions: Conceptualization, Y.Y.; methodology, D.L., S.W., X.Z.; investigation, D.L., X.W.; writing—original draft preparation, D.L.; writing—review and editing, Y.Y., J.R.S., J.Z.; visualization, D.L.; supervision, Y.Y.; project administration, Y.Y.; funding acquisition, Y.Y., J.R.S., D.L. All authors discussed the results and commented on the manuscript.

Funding: This research was funded by the National Key Research and Development Program of China (Grant No. 2016YFC0600204), the National Natural Science Foundation of China (Grant Nos. 41590621 and 41672041), the Fundamental Research Funds for National Universities, China University of Geosciences (Wuhan), and the US National Science Foundation (Grant No. EAR14-16979 to JRS).

Acknowledgments: We are grateful for the discussion from Xiang Wu and Xinzhuo Guo.

Conflicts of Interest: The authors declare no conflict of interest.

References

- Kohlstedt, D.L.; Keppler, H.; Rubie, D.C. Solubility of water in the α , β and γ phases of $(\text{Mg,Fe})_2\text{SiO}_4$. *Contrib. Mineral. Petrol.* **1996**, *123*, 345–357. [CrossRef]
- Smyth, J.R.; Frost, D.J.; Nestola, F.; Holl, C.M.; Bromiley, G.; Frost, D. Olivine hydration in the deep upper mantle: Effects of temperature and silica activity. *Geophys. Res. Lett.* **2006**, *33*, 311–324. [CrossRef]
- Litasov, K.D.; Ohtani, E.; Kagi, H.; Jacobsen, S.; Ghosh, S. Temperature dependence and mechanism of hydrogen incorporation in olivine at 12.5–14.0 GPa. *Geophys. Res. Lett.* **2007**, *34*, 16314. [CrossRef]
- Bali, E.; Bolfan-Casanova, N.; Koga, K.T. Pressure and temperature dependence of H solubility in forsterite: An implication to water activity in the Earth interior. *Earth Planet. Sci. Lett.* **2008**, *268*, 354–363. [CrossRef]
- Ye, Y.; Schwering, R.A.; Smyth, J.R. Effects of Hydration on Thermal Expansion of Forsterite, Wadsleyite, and Ringwoodite. *Am. Mineral.* **2009**, *94*, 899–904. [CrossRef]
- Otsuka, K.; Karato, S.-I. Control of the water fugacity at high pressures and temperatures: Applications to the incorporation mechanisms of water in olivine. *Phys. Earth Planet. Inter.* **2011**, *189*, 27–33. [CrossRef]
- Férot, A.; Bolfan-Casanova, N. Water storage capacity in olivine and pyroxene to 14 GPa: Implications for the water content of the Earth's upper mantle and nature of seismic discontinuities. *Earth Planet. Sci. Lett.* **2012**, *349–350*, 218–230. [CrossRef]
- Chang, Y.-Y.; Hsieh, W.-P.; Tan, E.; Chen, J. Hydration-reduced lattice thermal conductivity of olivine in Earth's upper mantle. *Proc. Natl. Acad. Sci. USA* **2017**, *114*, 4078–4081. [CrossRef]
- Wang, D.; Mookherjee, M.; Xu, Y.; Karato, S.-I. The effect of water on the electrical conductivity of olivine. *Nature* **2006**, *443*, 977–980. [CrossRef]
- Mei, S.; Kohlstedt, D.L. Influence of water on plastic deformation of olivine aggregates: 1. Diffusion creep regime. *J. Geophys. Res. Space Phys.* **2000**, *105*, 21457–21469. [CrossRef]
- Costa, F.; Chakraborty, S. The effect of water on Si and O diffusion rates in olivine and implications for transport properties and processes in the upper mantle. *Phys. Earth Planet. Inter.* **2008**, *166*, 11–29. [CrossRef]
- Hier-Majumder, S.; Anderson, I.M.; Kohlstedt, D.L. Influence of protons on Fe-Mg interdiffusion in olivine. *J. Geophys. Res. Space Phys.* **2005**, *110*, 110. [CrossRef]
- Fei, H.; Wiedenbeck, M.; Yamazaki, D.; Katsura, T. Small effect of water on upper-mantle rheology based on silicon self-diffusion coefficients. *Nature* **2013**, *498*, 213–215. [CrossRef] [PubMed]
- Fei, H.; Wiedenbeck, M.; Yamazaki, D.; Katsura, T. No effect of water on oxygen self-diffusion rate in forsterite. *J. Geophys. Res. Solid Earth* **2014**, *119*, 7598–7606. [CrossRef]

15. Fei, H.; Koizumi, S.; Sakamoto, N.; Hashiguchi, M.; Yurimoto, H.; Marquardt, K.; Miyajima, N.; Katsura, T. Mg lattice diffusion in iron-free olivine and implications to conductivity anomaly in the oceanic asthenosphere. *Earth Planet. Sci. Lett.* **2018**, *484*, 204–212. [[CrossRef](#)]
16. Manghnani, M.H.; Hushur, A.; Smyth, J.R.; Nestola, F.; Dera, P.; Sekar, M.; Amulele, G.; Frost, D.J. Compressibility and structural stability of two variably hydrated olivine samples (Fo₉₇Fa₃) to 34 GPa by X-ray diffraction and Raman spectroscopy. *Am. Miner.* **2013**, *98*, 1972–1979. [[CrossRef](#)]
17. Beran, A.; Putnis, A. A model of the OH positions in olivine, derived from infrared-spectroscopic investigations. *Phys. Chem. Miner.* **1983**, *9*, 57–60. [[CrossRef](#)]
18. Bai, Q.; Kohlstedt, D.L. Substantial hydrogen solubility in olivine and implications for water storage in the mantle. *Nature* **1992**, *357*, 672–674. [[CrossRef](#)]
19. Bai, Q.; Kohlstedt, D. Effects of chemical environment on the solubility and incorporation mechanism for hydrogen in olivine. *Phys. Chem. Miner.* **1993**, *19*, 460–471. [[CrossRef](#)]
20. Demouchy, S.; Mackwell, S. Water diffusion in synthetic iron-free forsterite. *Phys. Chem. Miner.* **2003**, *30*, 486–494. [[CrossRef](#)]
21. Zhao, Y.-H.; Ginsberg, S.B.; Kohlstedt, D.L. Solubility of hydrogen in olivine: Dependence on temperature and iron content. *Contrib. Mineral. Petrol.* **2004**, *147*, 155–161. [[CrossRef](#)]
22. Kohlstedt, D.L. The Role of Water in High-Temperature Rock Deformation. *Rev. Mineral. Geochem.* **2006**, *62*, 377–396. [[CrossRef](#)]
23. Deligne, N.I.; Mosenfelder, J.L.; Asimow, P.D.; Rossman, G.R. Hydrogen incorporation in olivine from 2–12 GPa. *Am. Miner.* **2006**, *91*, 285–294.
24. Hushur, A.; Manghnani, M.H.; Smyth, J.R.; Nestola, F.; Frost, D.J. Crystal chemistry of hydrous forsterite and its vibrational properties up to 41 GPa. *Am. Miner.* **2009**, *94*, 751–760. [[CrossRef](#)]
25. Karato, S.-I. Theory of isotope diffusion in a material with multiple species and its implications for hydrogen-enhanced electrical conductivity in olivine. *Phys. Earth Planet. Inter.* **2013**, *219*, 49–54. [[CrossRef](#)]
26. Karato, S.-I. Some notes on hydrogen-related point defects and their role in the isotope exchange and electrical conductivity in olivine. *Phys. Earth Planet. Inter.* **2015**, *248*, 94–98. [[CrossRef](#)]
27. O'Neill, H.S.C.; Matveev, S.; Ballhaus, C.; Taylor, W.R.; Green, D.H. Effect of Silica Activity on OH[−] IR Spectra of Olivine: Implications for Low-*a*SiO₂ Mantle Metasomatism. *J. Petrol.* **2001**, *42*, 721–729.
28. Berry, A.J.; Hermann, J.; O'Neill, H.S.; Foran, G.J.; Hermann, J. Fingerprinting the water site in mantle olivine. *Geology* **2005**, *33*, 869. [[CrossRef](#)]
29. O'Neill, H.S.; Hermann, J.; Hauri, E.H.; Kovács, I.; O'Neill, H.S. Site-specific infrared O-H absorption coefficients for water substitution into olivine. *Am. Miner.* **2010**, *95*, 292–299.
30. Umemoto, K.; Wentzcovitch, R.M.; Hirschmann, M.M.; Kohlstedt, D.L.; Withers, A.C. A first-principles investigation of hydrous defects and IR frequencies in forsterite: The case for Si vacancies. *Am. Miner.* **2011**, *96*, 1475–1479. [[CrossRef](#)]
31. Balan, E.; Ingrin, J.; Delattre, S.; Kovács, I.; Blanchard, M. Theoretical infrared spectrum of OH-defects in forsterite. *Eur. J. Mineral.* **2011**, *23*, 285–292. [[CrossRef](#)]
32. Xue, X.; Turner, D.; Lorocho, D.; Kanzaki, M. Hydrogen incorporation mechanisms in forsterite: New insights from 1 H and 29 Si NMR spectroscopy and first-principles calculation. *Am. Miner.* **2017**, *102*, 519–536. [[CrossRef](#)]
33. Qin, T.; Wentzcovitch, R.; Umemoto, K. Ab initio study of water speciation in forsterite. *Am. Miner.* **2018**, *103*, 692–699. [[CrossRef](#)]
34. Yang, Y.; Liu, W.; Qi, Z.; Wang, Z.; Smyth, J.R.; Xia, Q. Re-configuration and interaction of hydrogen sites in olivine at high temperature and high pressure. *Am. Mineral.* **2019**, *104*, 878–889. [[CrossRef](#)]
35. Padrón-Navarta, J.A.; Hermann, J.; O'Neill, H.S.C. Site-specific hydrogen diffusion rates in forsterite. *Earth Planet. Sci. Lett.* **2014**, *392*, 100–112. [[CrossRef](#)]
36. Kohn, S.C.; Brooker, R.A.; Lemaire, C. The effect of silica activity on the incorporation mechanisms of water in synthetic forsterite: A polarised infrared spectroscopic study. *Contrib. Mineral. Petrol.* **2004**, *147*, 48–57. [[CrossRef](#)]
37. Berry, A.J.; O'Neill, H.S.; Hermann, J.; Scott, D.R.; Hermann, J. The infrared signature of water associated with trivalent cations in olivine. *Earth Planet. Sci. Lett.* **2007**, *261*, 134–142. [[CrossRef](#)]
38. Berry, A.J.; Walker, A.M.; Hermann, J.; O'Neill, H.S.; Foran, G.J.; Gale, J.D.; Hermann, J. Titanium substitution mechanisms in forsterite. *Chem. Geol.* **2007**, *242*, 176–186. [[CrossRef](#)]

39. Grant, K.; Brooker, R.; Kohn, S.; Wood, B.; Kohn, S. The effect of oxygen fugacity on hydroxyl concentrations and speciation in olivine: Implications for water solubility in the upper mantle. *Earth Planet. Sci. Lett.* **2007**, *261*, 217–229. [[CrossRef](#)]
40. Walker, A.M.; Hermann, J.; Berry, A.J.; O'Neill, H.S.C.; Walker, A.; Berry, A. Three water sites in upper mantle olivine and the role of titanium in the water weakening mechanism. *J. Geophys. Res. Space Phys.* **2007**, *112*, 05211. [[CrossRef](#)]
41. Yang, X.-Z.; Keppler, H. In-situ infrared spectra of OH in olivine to 1100 °C. *Am. Miner.* **2011**, *96*, 451–454. [[CrossRef](#)]
42. Ingrin, J.; Kovács, I.; Deloule, E.; Balan, E.; Blanchard, M.; Kohn, S.C.; Hermann, J. Identification of hydrogen defects linked to boron substitution in synthetic forsterite and natural olivine. *Am. Miner.* **2014**, *99*, 2138–2141. [[CrossRef](#)]
43. Padrón Navarta, J.A.; Hermann, J. A subsolidus olivine water solubility equation for the Earth's upper mantle. *JGR Solid Earth* **2017**, *122*, 9862–9880. [[CrossRef](#)]
44. Crépeisson, C.; Blanchard, M.; Bureau, H.; Sanloup, C.; Withers, A.C.; Khodja, H.; Surblé, S.; Raepsaet, C.; Béneut, K.; Leroy, C.; et al. Clumped fluoride-hydroxyl defects in forsterite: Implications for the upper-mantle. *Earth Planet. Sci. Lett.* **2014**, *390*, 287–295. [[CrossRef](#)]
45. Grant, K.J.; Kohn, S.C.; Brooker, R.A. Solubility and partitioning of water in synthetic forsterite and enstatite in the system $\text{MgO-SiO}_2\text{-H}_2\text{O} \pm \text{Al}_2\text{O}_3$. *Contrib. Mineral. Petrol.* **2006**, *151*, 651–664. [[CrossRef](#)]
46. Withers, A.; Hirschmann, M.; Tenner, T. The effect of Fe on olivine H_2O storage capacity: Consequences for H_2O in the martian mantle. *Am. Miner.* **2011**, *96*, 1039–1053. [[CrossRef](#)]
47. Ingrin, J.; Liu, J.; Depecker, C.; Kohn, S.C.; Balan, E.; Grant, K.J. Low-temperature evolution of OH bands in synthetic forsterite, implication for the nature of H defects at high pressure. *Phys. Chem. Miner.* **2013**, *40*, 499–510. [[CrossRef](#)]
48. Kudoh, Y.; Kuribayashi, T.; Kagi, H.; Inoue, T. Cation vacancy and possible hydrogen positions in hydrous forsterite, $\text{Mg}_{1.985}\text{Si}_{0.993}\text{H}_{0.06}\text{O}_4$, synthesized at 13.5 GPa and 1300 °C. *J. Mineral. Petrol. Sci.* **2006**, *101*, 265–269. [[CrossRef](#)]
49. Tollan, P.M.E.; Smith, R.; O'Neill, H.S.; Hermann, J. The responses of the four main substitution mechanisms of H in olivine to H_2O activity at 1050 °C and 3 GPa. *Prog. Earth Planet. Sci.* **2017**, *4*, 200. [[CrossRef](#)]
50. Gillet, P.; Richet, P.; Guyot, F.; Fiquet, G. High-temperature thermodynamic properties of forsterite. *J. Geophys. Res. Space Phys.* **1991**, *96*, 11805. [[CrossRef](#)]
51. Liu, D.; Pang, Y.; Ye, Y.; Jin, Z.; Smyth, J.R.; Yang, Y.; Zhang, Z.; Wang, Z. In-situ high-temperature vibrational spectra for synthetic and natural clinohumite: Implications for dense hydrous magnesium silicates in subduction zones. *Am. Miner.* **2019**, *104*, 53–63. [[CrossRef](#)]
52. Dorogokupets, P.I.; Oganov, A.R. Ruby, metals, and MgO as alternative pressure scales: A semiempirical description of shock-wave, ultrasonic, x-ray, and thermochemical data at high temperatures and pressures. *Phys. Rev. B* **2007**, *75*, 024115. [[CrossRef](#)]
53. Dorogokupets, P.; Dymshits, A.; Sokolova, T.; Danilov, B.; Litasov, K. The equations of state of forsterite, wadsleyite, ringwoodite, akimotoite, MgSiO_3 -perovskite, and postperovskite and phase diagram for the Mg_2SiO_4 system at pressures of up to 130 GPa. *Russ. Geol. Geophys.* **2015**, *56*, 172–189. [[CrossRef](#)]
54. Reynard, B.; Caracas, R. D/H isotopic fractionation between brucite $\text{Mg}(\text{OH})_2$ and water from first-principles vibrational modeling. *Chem. Geol.* **2009**, *262*, 159–168. [[CrossRef](#)]
55. Liu, Q.; Tossell, J.A.; Liu, Y. On the proper use of the Bigeleisen–Mayer equation and corrections to it in the calculation of isotopic fractionation equilibrium constants. *Geochim. Cosmochim. Acta* **2010**, *74*, 6965–6983. [[CrossRef](#)]
56. Marcondes, M.L.; Wentzcovitch, R.M.; Assali, L.V. Importance of van der Waals interaction on structural, vibrational, and thermodynamic properties of NaCl. *Solid State Commun.* **2018**, *273*, 11–16. [[CrossRef](#)]
57. Yang, Y.; Wang, Z.; Smyth, J.R.; Liu, J.; Xia, Q. Water effects on the anharmonic properties of forsterite. *Am. Miner.* **2015**, *100*, 2185–2190. [[CrossRef](#)]
58. Withers, A.C.; Bureau, H.; Raepsaet, C.; Hirschmann, M.M. Calibration of infrared spectroscopy by elastic recoil detection analysis of H in synthetic olivine. *Chem. Geol.* **2012**, *334*, 92–98. [[CrossRef](#)]
59. Nakamoto, K.; Margoshes, M.; Rundle, R.E. Stretching Frequencies as a Function of Distances in Hydrogen Bonds. *J. Am. Chem. Soc.* **1955**, *77*, 6480–6486. [[CrossRef](#)]

60. Libowitzky, E. Correlation of O-H stretching frequencies and O-H ... O hydrogen bond lengths in minerals. *Monatshefte. Fiir. Chemie.* **1999**, *130*, 1047–1059.
61. Balan, E.; Blanchard, M.; Lazzeri, M.; Ingrin, J. Contribution of interstitial OH groups to the incorporation of water in forsterite. *Phys. Chem. Miner.* **2014**, *41*, 105–114. [[CrossRef](#)]
62. Koch-Müller, M.; Matsyuk, S.S.; Rhede, D.; Wirth, R.; Khisina, N. Hydroxyl in mantle olivine xenocrysts from the Udachnaya kimberlite pipe. *Phys. Chem. Miner.* **2006**, *33*, 276–287. [[CrossRef](#)]
63. Cynn, H.; Hofmeister, A.M.; Burnley, P.C.; Navrotsky, A. Thermodynamic properties and hydrogen bonding speciation from vibrational spectra of dense hydrous magnesium silicates. *Phys. Chem. Miner.* **1996**, *23*, 361–376. [[CrossRef](#)]
64. Holland, T.J.B.; Powell, R. An internally consistent thermodynamic data set for phases of petrological interest. *J. Metamorph. Geol.* **1998**, *163*, 309–343.
65. Okada, T.; Narita, T.; Nagai, T.; Yamanaka, T. Comparative Raman spectroscopic study on ilmenite-type MgSiO_3 (akimotoite), MgGeO_3 , and MgTiO_3 (geikielite) at high temperatures and high pressures. *Am. Miner.* **2008**, *93*, 39–47. [[CrossRef](#)]
66. Chopelas, A. Single crystal Raman spectra of forsterite, fayalite, and monticellite. *Am. Mineral.* **1991**, *76*, 1101–1109.
67. Hofmeister, A.M. Single-crystal absorption and reflection infrared spectroscopy of forsterite and fayalite. *Phys. Chem. Miner.* **1987**, *14*, 499–513. [[CrossRef](#)]
68. Kieffer, S.W. Thermodynamics and lattice vibrations of minerals: 3. Lattice dynamics and an approximation for minerals with application to simple substances and framework silicates. *Rev. Geophys.* **1979**, *17*, 35. [[CrossRef](#)]
69. Polyakov, V.B. On anharmonic and pressure corrections to the equilibrium isotope constants for minerals. *Geochim. Cosmochim. Acta.* **1988**, *62*(18), 3077–3085. [[CrossRef](#)]
70. Polyakov, V.; Horita, J.; Cole, D.; Polyakov, V. Pressure effects on the reduced partition function ratio for hydrogen isotopes in water. *Geochim. Cosmochim. Acta* **2006**, *70*, 1904–1913. [[CrossRef](#)]
71. Wu, Z.; Huang, F.; Huang, S. Isotope fractionation induced by phase transformation: First-principles investigation for Mg_2SiO_4 . *Earth Planet. Sci. Lett.* **2015**, *409*, 339–347. [[CrossRef](#)]



© 2019 by the authors. Licensee MDPI, Basel, Switzerland. This article is an open access article distributed under the terms and conditions of the Creative Commons Attribution (CC BY) license (<http://creativecommons.org/licenses/by/4.0/>).